From Neural Network Decisions to Training Cases: An Exact Account via Case-Based Decision Theory

Manli Yan, Yuebin Lin, Yaowen Yu (Corresponding author), Yong Zhao
Huazhong University of Science and Technology
Wuhan, China
d202481469@hust.edu.cn, m202473690@hust.edu.cn
yaowen_yu@hust.edu.cn, zhiwei98530@hust.edu.cn

Preprint

arXiv:2607.11347v1 [cs.AI] 13 Jul 2026

Abstract

Neural networks increasingly guide decisions in high-stakes domains such as medical diagnosis, credit approval, and energy bidding. Audit in these settings requires case-level evidence: which training cases support an action and what outcomes they carried. Case-based decision theory (CBDT) formalizes this reasoning by aggregating outcome support from remembered cases. We show that an OLS action readout fitted on a fixed neural representation admits an exact case-based decomposition. Each action score is a weighted sum of training-case returns, with coefficients determined by empirical Gram geometry. We identify a sufficient regime for CBDT similarity semantics; outside it, the coefficients should generally be treated as signed Gram-geometric influence. The decomposition yields audit signals that trace scores to training cases, measure action coherence, and identify weak support. Across synthetic CBDT, PJM, Adult Income, and Default Credit tasks, the method recovers case-level preference structure and achieves the highest mean Top-30 consistency among compared attribution baselines, while remaining competitive on support reconstruction. The audit requires only fitting an OLS top-layer probe, without retraining the representation or accessing the original optimization trajectory; probe fidelity is measured by score reconstruction.

Keywords: case-based decision theory; neural network interpretability; training-data attribution; case-based reasoning; representation geometry; post-training audit.

1 Introduction

Modern neural networks increasingly guide decisions in high-stakes domains such as medical diagnosis, credit approval, and energy bidding. In these settings, a model score often functions as evidence for one action over another. This shift changes what an explanation must provide: users need to know what evidence supports an action preference and whether that evidence is reliable enough to be inspected, contested, or used to guide intervention [1, 2]. Feature-attribution methods, among the most widely used tools for neural network interpretability, address part of this requirement by locating input variables that affect a prediction, including local surrogate explanations and Shapley-style attributions [3, 4]. Decision audit, however, also requires training-case evidence: which past cases matter, what returns or outcomes they carried, and how they shape the current action choice.

CBDT is a natural starting point because it makes case evidence explicit. It models a familiar pattern in human decision making: current actions are evaluated by comparing the present problem with remembered cases and aggregating the outcome support carried by similar cases [5, 6, 7, 8]. In decision-theoretic terms, CBDT formalizes case-based rationality: memory, similarity, and outcome support jointly constrain preferences without requiring a fully specified probabilistic model. This structure also makes the evidence behind a decision explicit and inspectable, which is valuable for audit. Case-based neural architectures make exemplars, prototypes, or retrieved neighbors explicit through prototype layers, matching mechanisms, memory modules, or nearest-neighbor retrieval [9, 10, 11, 12, 13]. Standard neural networks also learn from past examples, but this experience is absorbed into learned parameters rather than exposed as an inspectable case memory. The connection between a deployed neural decision and its relevant training cases therefore remains indirect: it is unclear how, or under what semantics, training-case evidence can be recovered after training.

This question connects three strands of work: representation analysis, training-data attribution, and case-based neural architectures. Representation analysis and linear probes show that learned neural spaces often make task-relevant information linearly accessible [14, 15], motivating the fixed-representation readout setting studied here. Training-data attribution traces predictions to training examples through perturbation, optimization-path, valuation, or influence-based approximations [16, 17, 18, 19, 20, 21, 22, 23, 24, 25]. Recent work extends data attribution to non-decomposable objectives and large generative models, while emphasizing that attribution quality depends on the evaluation task [26, 27, 28]. Formal analyses of prototype networks also show that displayed cases need not constitute sufficient explanations [29]. Our focus is complementary: an exact score decomposition and its CBDT semantic conditions for ordinary fixed-representation OLS readouts.

We connect CBDT with neural decision making and use this connection to make the training-case evidence behind neural action scores explicit and auditable. Our contributions are threefold.

- **An exact CBDT-style account of neural action scores.** For fixed-representation OLS readouts, we show that each action score is exactly an aggregation of training-case action returns. This gives users a direct route from a neural decision to the cases that raise, lower, or otherwise shape its score.
- **Semantics for case-based neural evidence.** We characterize when the induced case weights have CBDT similarity semantics and when they should instead be interpreted as signed Gram-geometric influence. This distinction prevents users from conflating influence with similarity and clarifies what retrieved cases mean.
- **A retraining-free decision audit framework.** We develop audit signals that identify influential cases, measure the coherence of their action evidence, and highlight weakly supported predictions. The audit requires only fitting an OLS top-layer probe, without retraining the representation or accessing the original optimization trajectory.

2 Background and Setup

2.1 Case-Based Decision Theory

CBDT models experience-based choice by evaluating actions through remembered cases, their similarity to the current problem, and their outcome support. In human case-based decision making, this makes preferences traceable to a structured relation among memory, similarity, and outcomes. This structure provides the conceptual basis for asking whether neural decisions can be audited through analogous training-case evidence.

Let P, A, and R denote the problem, action, and outcome spaces. A case is $c = (p_c, a_c, r_c)$, and a memory M is a multiset of cases. For the current problem p and candidate action a, CBDT defines the support as

$$U(a \mid M, p) = \sum_{c \in M} n(c, M)\, s\left(p, p_c\right)\, u\left(r_c, a\right), \qquad (1)$$

where $n(c, M)$ is the case frequency, $s\left(p, p_c\right)$ is problem-level similarity, and $u\left(r_c, a\right)$ is the outcome-based support contributed by that case. The CBDT decision maker selects

$$a^*(M, p) = \arg\max_{a \in A} U(a \mid M, p). \qquad (2)$$

Standard CBDT separates non-negative similarity from action support, making an action preference traceable to remembered cases and their outcomes. Neural models with explicit case-retrieval mechanisms implement this structure through prototypes, examples, or memory modules [9, 10, 11, 12]. For a standard fixed-representation linear readout without an explicit case memory, the central issue is when the OLS-induced case coefficients can be read as CBDT similarity weights and when they should instead be treated as signed Gram-geometric influence coefficients.

2.2 Fixed-Representation Linear Readouts

Consider a trained network with a representation map $\varphi(x) \in \mathbb{R}^H$ fixed after training. For each discrete action $a \in A$, the top-layer readout is linear in this representation:

$$Q(x, a) = v_a^\top \varphi(x). \tag{3}$$

If the readout includes an intercept, the constant coordinate is absorbed into $\varphi(x)$ and the notation is retained. Given training inputs $x_1, \ldots, x_n$, define the training representation matrix Φ and the empirical Gram matrix G as

$$\Phi = \begin{bmatrix} \varphi(x_1)^\top \\ \cdots \\ \varphi(x_n)^\top \end{bmatrix}, \quad G = \Phi^\top \Phi. \tag{4}$$

For each action a, let

$$\mathbf{r}_a = (r_{1,a}, \ldots, r_{n,a})^\top \tag{5}$$

denote the action-conditional return vector; each entry $r_i(a)$ is the return associated with the corresponding action and training problem. The squared-loss readout is

$$v_a = \arg\min_{v \in \mathbb{R}^H} \| \Phi v - \mathbf{r}_a \|_2^2 . \tag{6}$$

The main analysis assumes that the feature matrix Φ has full column rank. Equivalently, $n \geq H$ and the feature-side empirical Gram matrix G is invertible and symmetric positive definite [30]. We use the feature-side Gram matrix here; the sample-side kernel Gram matrix has a different dimension and plays a different role. If G is singular or ill-conditioned, Tikhonov regularization replaces the inverse by the regularized inverse defined below. For reference, the main notation is collected in Appendix A.

The analysis focuses on a standard post-training setting [14, 15]: after the representation has been trained, it is held fixed and equipped with an OLS top-layer probe. Within this fixed-representation readout, the decomposition is exact and the readout score can be audited directly through training-case evidence. The result does not claim that arbitrary end-to-end nonlinear training admits the same decomposition without this fixed-representation reduction. The analysis assumes observed or constructed action-conditional returns for all candidate actions. With factual-only outcomes, it instead applies to estimated returns and inherits the error of the corresponding outcome model.

3 Gram-Structured Case Influence

3.1 Canonical OLS-Induced Case-Influence Decomposition

This section derives the case-influence form of a fixed-representation OLS readout. We first derive the exact case-weighted form of each action score. The semantic interpretation of the resulting weights is addressed in Sec. 3.3.

$$\Phi^\top \Phi v_a = \Phi^\top \mathbf{r}_a. \tag{7}$$

When $G = \Phi^\top \Phi$ is invertible,

$$v_a = G^{-1} \Phi^\top \mathbf{r}_a. \tag{8}$$

Substituting Eq. (8) into the readout score gives

$$Q(x, a) = \varphi(x)^\top G^{-1} \Phi^\top \mathbf{r}_a = \sum_{i=1}^{n} \alpha_i(x) r_{i,a}, \tag{9}$$

where

$$\alpha_i(x) = \varphi(x)^\top G^{-1} \varphi(x_i). \tag{10}$$

Proposition 1 (Canonical case-influence decomposition) If the feature matrix has full column rank, the empirical Gram matrix is invertible. Then the OLS readout score for each action admits the case-weighted form in Eq. (9), with coefficients given by Eq. (10). The coefficient vector $\alpha(x)$ is the unique minimum-norm solution to the associated consistent linear system. Consistency follows because the transposed feature matrix has full row rank under the same assumption. It is therefore the canonical OLS-induced case-influence coefficient. The proof uses a standard convex-optimization argument [31] and is given in Appendix B.1.

When the empirical Gram matrix is singular or ill-conditioned, the same derivation gives the Tikhonov-regularized coefficient:

$$\alpha_\lambda(x) = \Phi (G + \lambda I_H)^{-1} \varphi(x). \tag{11}$$

The regularized coefficient converges to Eq. (10) whenever the empirical Gram matrix is invertible.

Remark on uniqueness: When $n > H$, the system $\Phi^\top \beta = \varphi(x)$ admits infinitely many solutions; $\alpha(x) = \Phi G^{-1} \varphi(x)$ is the one minimizing $\| \beta \|_2$. The decomposition in Eqs. (9) and (10) is the unique decomposition whose dual coefficient agrees with the OLS normal equation. A Lagrange-multiplier proof is in Appendix B.1.

Eq. (9) is the main case-influence representation used throughout the audit framework. It expresses each readout action score as an exact weighted sum of training-case returns, with weights determined by the empirical Gram geometry of the representation.

3.2 Coordinate Invariance

A useful invariance requirement for the case-influence coefficient is coordinate invariance: rewriting the same representation in another invertible linear basis must leave the coefficient unchanged. Let B be invertible and define $\varphi_B(x) = B\varphi(x)$. Then the unregularized OLS case gives the same coefficient:

$$\alpha_B(x) = \Phi_B \left(BGB^\top\right)^{-1} B\varphi(x) = \Phi G^{-1} \varphi(x) = \alpha(x). \tag{12}$$

Thus, the case-influence coefficient is an invariant property of the fixed-representation readout, tied to the represented linear function across coordinate bases. With regularization, invariance requires the regularization metric to transform with the representation. A fixed isotropic penalty generally breaks invariance under non-orthogonal reparameterizations. The algebraic proof and empirical check are given in Appendices B.2 and C.1.

3.3 A Sufficient Regime for CBDT Similarity

Eqs. (1) and (9) have the same aggregation form: both compute an action score by summing case returns with case-dependent weights, but this algebraic similarity does not imply identical semantics. CBDT uses non-negative similarity weights, whereas the OLS-induced coefficient is Gram-induced, signed, and unnormalized. A CBDT similarity interpretation therefore requires additional geometric conditions. If the representation is whitened so that

$$G = \Phi^\top \Phi = nI_H, \tag{13}$$

then

$$\alpha_i(x) = \frac{1}{n}\varphi(x)^\top \varphi\left(x_i\right). \tag{14}$$

If $G = nI_H$, the coefficient reduces in the original representation coordinates to the scaled inner product in Eq. (14). Whitening is therefore a transparent sufficient condition for this raw inner-product form, while a standard CBDT similarity interpretation additionally requires non-negativity on the relevant problem domain. Outside this sufficient regime, the coefficient remains a coordinate-invariant, potentially signed Gram-metric coefficient. This distinction motivates the signed-coefficient diagnostics below. Appendix B.3 gives the derivation, and Appendix C.1 verifies empirically that post-hoc invertible ZCA reparameterization leaves the unregularized coefficients unchanged.

4 Case-Influence Audit Signals

With Eq. (9), a readout score becomes case-level evidence. The resulting audit asks three questions: which training cases raise or lower an action score, whether the influential cases support a coherent action pattern, and whether the query is weakly supported by the training distribution. Because coefficients can be positive or negative, entropy and case-influence risk diagnostics are built from absolute influence mass, while signed contribution is retained for single-case auditing.

(i) Case audit score

For a test point and candidate action, each training-case contribution is

$$\psi_i(a, x) = \alpha_i(x) r_{i,a}. \tag{15}$$

Sorting cases by absolute contribution gives the most influential cases, while the sign of each contribution indicates whether that case raises or lowers the action score. Sorting by signed contribution isolates the strongest positive support, while sorting in ascending order highlights the strongest negative offsets. Inspecting the top cases can reveal whether the prediction is driven by nearby examples, a specific time period, a data source, or potential outliers.

(ii) Influence entropy for action coherence

Beyond individual case contributions, the audit also asks whether the most influential cases point to a coherent action pattern. Let $I_k(x, a)$ be the indices of the top-k training cases ranked by absolute contribution $|\psi_i(a, x)|$. With magnitude weight $m_i(a, x) = |\psi_i(a, x)|$, define the action distribution

$$\pi_k(b \mid x, a) = \frac{\sum_{i \in I_k(x,a)} m_i(a, x)\mathbf{1}\{a_i^* = b\} + \varepsilon/|A|}{\sum_{i \in I_k(x,a)} m_i(a, x) + \varepsilon}, \tag{16}$$

where $a_i^\star$ is the case-optimal action and $\varepsilon > 0$ is a numerical safeguard. The symmetric ε-smoothing makes $\pi_k(\cdot \mid x, a)$ a valid probability distribution, including when the selected influence mass is numerically zero. The influence entropy is

$$H_\alpha(x, a) = -\sum_{b \in A} \pi_k(b \mid x, a) \log \pi_k(b \mid x, a). \tag{17}$$

Low entropy means that the top-k influence mass is concentrated on cases favoring one action, whereas high entropy indicates that influential cases are spread across multiple case-optimal actions. Because the distribution is built from absolute influence mass, $H_\alpha(x, a)$ reports action coherence among influential cases and is separate from calibrated predictive probability.

(iii) Case-influence risk diagnostic

A neural decision is less well supported when its strongest training-case influences provide dispersed or conflicting action evidence. The case-influence risk diagnostic is designed to flag such weakly supported queries by combining the entropy in Eq. (17) with a local disagreement term among the strongest case influences. Let $T_{10}(x) = I_{10}(x, a_x)$ denote the ten cases with largest absolute contributions $|\psi_i(a_x, x)|$ to the selected action. Let q_x be the count distribution of case-optimal actions among $T_{10}(x)$:

$$q_x(b) = \frac{1}{10} \sum_{i \in T_{10}(x)} \mathbf{1}\{a_i^* = b\}, \tag{18}$$

and define the corresponding Gini disagreement as

$$D_{Gini}(x) = 1 - \sum_{b \in A} q_x(b)^2. \tag{19}$$

The case-influence risk score is

$$O_\alpha(x) = H_\alpha\left(x, a_x\right) + \gamma D_{Gini}(x). \tag{20}$$

Here $a_x = \arg\max_{a \in A} Q(x, a)$ denotes the action selected by the readout. The experiments set γ to 1. Larger values indicate that the top-influence cases provide less coherent action support, either through dispersed influence mass or disagreement among the strongest local cases. This diagnostic is conceptually complementary to representation- and

confidence-based shift diagnostics because it measures mismatch through case-influence geometry. It is evaluated in Sec. 5.5, with the full drift grid reported in Appendix C.4.

5 Experiments

5.1 Experimental Setup

The experiments evaluate three claims: whether the decomposition recovers known case-preference structure, whether it ranks influential training cases reliably, and whether its audit signals remain useful after training. The evaluation covers a synthetic CBDT generator, PJM bidding with real load observations, UCI Adult Income proxy decisions, and UCI Default Credit proxy decisions, spanning controlled ground truth, time-series energy bidding, and income- and credit-risk audit settings. Across all tasks, a representation is trained and fixed, an OLS top-layer probe is fitted, and results are reported over five random seeds with means and 95% confidence intervals. We report four types of evidence: support reconstruction, case-ranking quality, audit-time cost, and diagnostic AUC. Baselines cover influence-function attribution, representer-point attribution, trajectory-based attribution, and a geometry-only inner-product baseline. The UCI proxy returns serve methodological audit evaluation; deployment policy design requires an independent return specification.

5.2 Recovering Known Case-Preference Structure

We first test whether the readout recovers a known case-support mechanism. The synthetic CBDT generator contains twenty cases, three actions, Gaussian similarity, and known support values. The generator produces 500 training samples and 200 test samples, so both the CBDT optimal action and the true action-support scores are directly observable. The fixed-representation OLS readout reaches 96.0% test agreement with the CBDT optimal action, and its reconstructed action-support scores correlate strongly with the true CBDT supports across the three actions. Figure 1 visualizes this recovery at the decision and support levels: the explicit CBDT rule and the neural readout induce closely aligned decision regions, and the reconstructed neural support lies near the true CBDT support for all three actions. This controlled result supports the central premise of the paper: a fixed-representation OLS readout can recover a case-aggregation structure behind its action scores.

5.3 Comparison with Training-Data Attribution Baselines

To evaluate whether the proposed coefficient identifies decision-relevant training cases, we compare it with representative training-data attribution baselines: Influence Functions [16], Representer Point Selection [17], TracIn [19], and an inner-product baseline corresponding to the sufficient similarity regime in Sec. 3.3. Figure 2 summarizes the comparison, and Table 1 reports the corresponding mean scores and confidence intervals. We evaluate ranking quality using Top-30 action consistency and Pearson correlation with CBDT ground-truth case contributions.

Method	Top-30 cons. (prop.)	Pearson r
Ours (α)	**0.941±0.030**	**0.368±0.172**
Representer Point	0.667±0.128	0.090±0.080
TracIn	0.671±0.129	0.089±0.156
Influence Functions	0.909±0.043	0.295±0.123
Inner-product	0.697±0.092	0.277±0.086

Table 1: Attribution baselines. Values are means with 95% confidence intervals over five seeds; bold marks the best mean.

The proposed coefficient achieves the highest Top-30 action consistency, outperforming Influence Functions, Representer Point, TracIn, and the inner-product baseline on Top-30 action consistency. Its case-level Pearson correlation has an overlapping 95% confidence interval with Influence Functions and a higher mean than Representer Point and TracIn. The larger variance of Pearson reflects the difficulty of matching exact per-case contribution magnitudes across seeds, whereas Top-30 consistency more directly evaluates whether the dominant action-supporting cases are retrieved. Figure 2 shows that the proposed coefficient gives the strongest top-ranked case consistency while retaining competitive support reconstruction.

The proposed coefficient yields stronger case-level consistency with higher per-query cost; Appendix D reports the timing convention and relative-cost comparison. In absolute terms, the cached online audit averages 58.6 ms per query in our implementation, compared with sub-millisecond baselines, so the method trades higher latency for stronger decision-relevant case retrieval without retraining or access to the original optimization trajectory.

5.4 Real-Data Audit Tasks with Proxy Returns: PJM and UCI

The next experiments test whether the Gram-structured decomposition remains informative when neural decisions are made on real observed covariates with controlled or proxy return specifications. In PJM, real half-hourly load observations define a rolling-window three-action bidding problem [32], while synthetic prices make action-specific returns observable for audit. This setting allows the neural network policy and the explicit CBDT decision maker to be compared under the same return structure. The two decision rules agree on 3221 of 3358 test decisions, and Figure 3 shows that the 137 disagreements concentrate in the load-transition region where decision margins are small. The support correlations further indicate where the audit is most reliable: conservative and moderate actions align strongly with CBDT support, while the weaker aggressive-action alignment reflects the higher-risk region

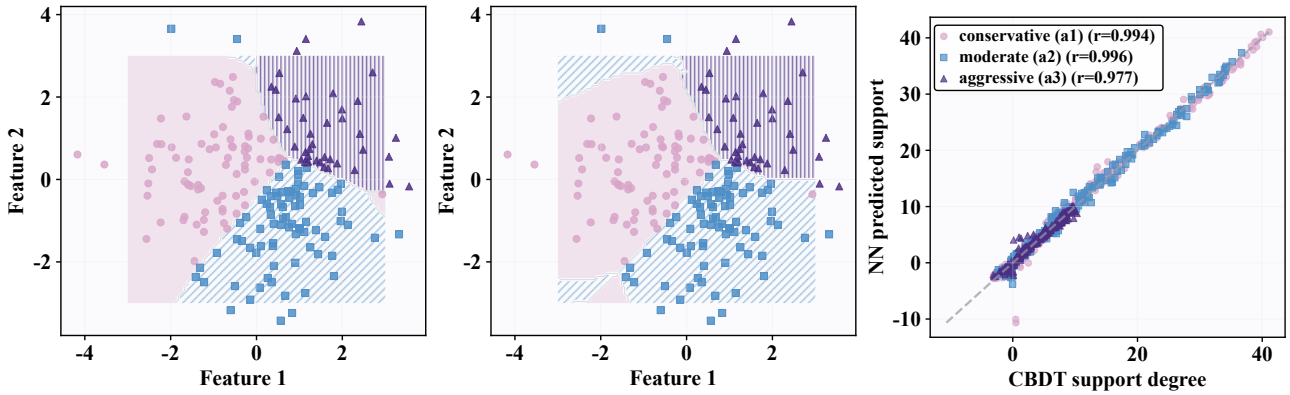

(a) CBDT decision boundary (b) Neural network decision boundary (c) Support reconstruction

Figure 1: Synthetic CBDT recovery. The neural readout matches the CBDT decision regions and support scores. This supports the claim that fixed-representation OLS scores can expose case aggregation.

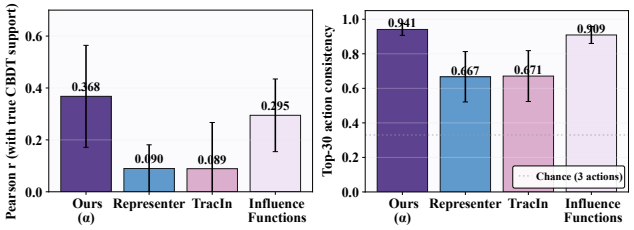

(a) Support reconstruction (b) Top-30 consistency

Figure 2: Training-data attribution comparison. The proposed coefficient gives the strongest Top-30 consistency with competitive support reconstruction. The result shows that the Gram-derived coefficient better retrieves decision-relevant cases than standard attribution baselines in this controlled setting.

where returns are more sensitive to boundary cases and price-driven variation. This identifies the aggressive action as the one requiring closer audit attention. The fixed-representation OLS reconstruction also closely matches the trained network action scores, with action-wise correlations of 0.9998, 0.9972, and 0.9592. These are OLS–NN probe-fidelity correlations ρ_{recon}, distinct from the CBDT-support alignment ρ_{support} reported in Fig. 3(b).

The same audit pipeline is then evaluated on two different proxy decision problems: income-based approval on Adult Income and default-risk exposure control on Default Credit. Adult Income is cast as an approval task with conservative rejection, standard approval, and aggressive high-limit approval; the proxy returns are specified in Appendix C.5. This task reaches network-CBDT behavioral agreement of 0.9408, with neural-network accuracy of 0.7982. Default Credit concerns repayment risk and credit exposure adjustment. Using the Yeh and Lien dataset [33] from the UCI repository [34], the proxy actions correspond to reject or decrease exposure, standard approval, and increase exposure. This task obtains network-CBDT agreement of 0.875, with OLS reconstruction correlations of 0.998, 0.956, and 0.998 across the three actions. Figure 4 connects these two audits: Adult Income shows close agreement between network and CBDT decisions in an income-approval setting, while Default Credit shows that the decomposition remains accurate under a different risk structure, with the weaker standard-approval reconstruction marking the most ambiguous action. Additional Default Credit decomposition details are given in Appendix C.6.

5.5 Case-Influence Diagnostics

This section evaluates whether the case-influence coefficients provide useful post-training diagnostics. Three uses are considered: interpreting signed influence, tracing an individual neural decision to concrete training cases, and identifying decisions whose case evidence is weak or internally inconsistent.

The first diagnostic concerns the meaning of signed coefficients. Here, positive and negative refer to the sign of $\alpha_i(x)$; whether a case raises or lowers the inspected action score is determined by the signed contribution $\psi_i(a, x) = \alpha_i(x) r_i(a)$. In PJM, the sign of a coefficient is linked to where the corresponding training case lies relative to the current test input in the fixed representation space. Across 50 PJM test inputs, the top-5 positive-coefficient cases have a mean standardized representation distance of 0.44 ± 0.04, compared with 3.30 ± 0.16 for the top-5 negative-coefficient cases, a 7.5-fold difference. The positive-coefficient group also agrees with the predicted action more often, and its mean absolute coefficient magnitude is about 3.7 times larger than that of the negative-coefficient group. In PJM, positive coefficients mainly identify nearby cases in the learned representation, while negative coefficients behave as far-field Gram correction terms; the aggregate statistics over the 50 test inputs are included in Appendix C.2.

The second diagnostic traces one PJM prediction to ranked training cases. For a representative test input where the network selects action 1, Figure 5 shows positive- and negative-coefficient cases in the fixed representation space

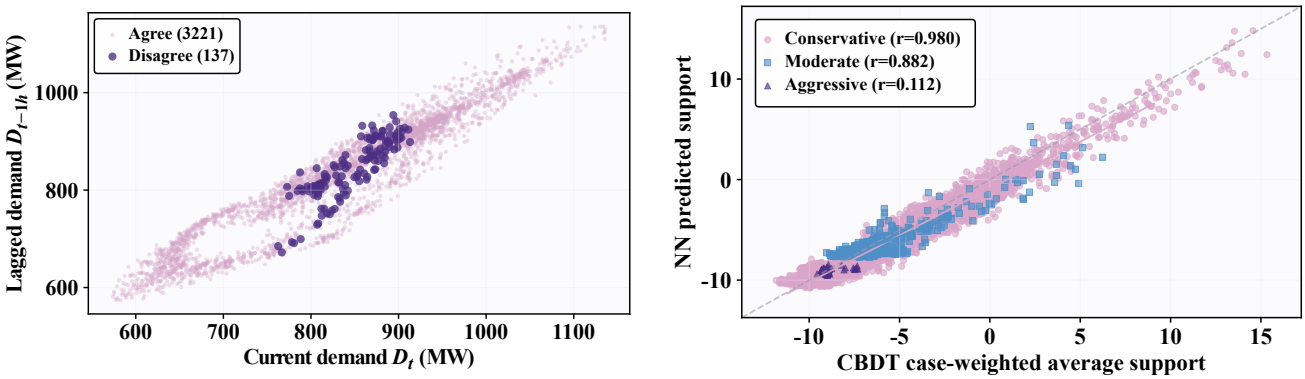

(a) NN-CBDT decision agreement

(b) Case-weighted average support

Figure 3: PJM audit. Neural and CBDT decisions agree on most test inputs, with disagreements concentrated near low-margin load transitions. Strong support alignment for the conservative and moderate actions shows where the case decomposition is reliable, while weaker aggressive-action alignment identifies the part needing closer audit.

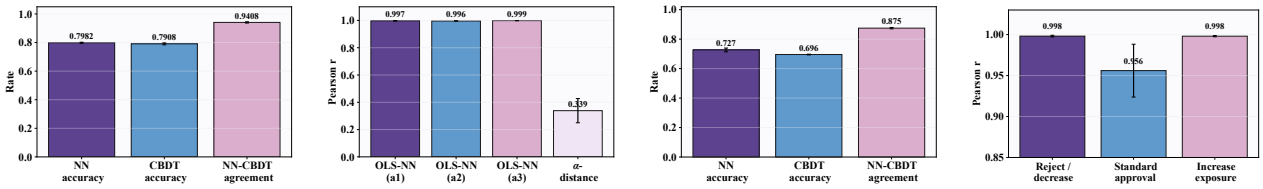

(a) Adult behavior

(b) Adult recon.

(c) Default behavior

(d) Default recon.

Figure 4: UCI proxy-decision audits. Adult Income and Default Credit show high network-CBDT agreement and strong OLS reconstruction. The weaker Default Credit standard-approval action shows that the audit can identify the least faithfully reconstructed action.

together with their action agreement. The strongest positive-coefficient cases lie near the test input and mostly support the selected action, matching the aggregate pattern above. The strongest negative-coefficient cases are farther away and adjust the score through the Gram-based decomposition. This single-decision audit shows how ranked training cases assemble a prediction: the sign and magnitude of each case coefficient indicate whether that case raises, lowers, or offsets the readout score. The full ranked list for this test input is given in Appendix C.3.

The third diagnostic uses case influence to assess whether a test input is reliably supported by the training distribution. A weakly supported input tends to retrieve influential cases with dispersed or conflicting action evidence, so the case-influence risk score is designed to detect changes in local case geometry and action-evidence structure. Under covariate-axis scale shift, the case-influence score improves incorrect-prediction AUC over a standard network-margin baseline, with the clearest paired-seed gains occurring under larger covariate shifts; the complete comparisons are reported in Appendix C.4. This improvement suggests that the score captures changes in local influential-case geometry and action-evidence structure, especially when variance or covariance shifts disrupt the support pattern around the test input. The strongest gains occur under covariate shift, where the influential-case neighborhood changes and the network margin loses diagnostic resolution.

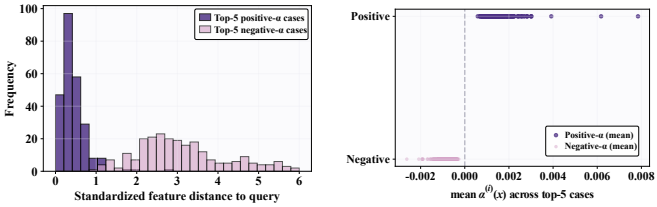

(a) Distance distribution

(b) Coefficient distribution

Figure 5: Geometry of signed case influence. Positive-coefficient cases cluster near the test input and mostly support the selected action, while negative-coefficient cases are farther away. The separation gives the signed coefficient an interpretable audit role rather than treating all retrieved cases as uniformly supportive.

This pattern gives the score a distinct role among shift diagnostics. It is most useful under covariate shifts, where influential-case neighborhoods change; under mean or variance shifts, it should be viewed as complementary rather than uniformly superior to margin-based detection.

6 Conclusion and Discussion

Taken together, this paper makes the training-case basis of neural network decisions algebraically explicit. For fixed-representation OLS readouts, each action score is an exact aggregation of training-case returns, with coefficients determined by empirical Gram geometry. This gives users a direct post-training route from a neural decision to the training cases that raise, lower, or offset it. The interpretation has clear boundaries: only under a sufficient whitening and non-negativity regime do the coefficients behave like CBDT similarity weights; otherwise they are signed Gram-geometric influence terms. As a result, the framework provides a practical post-training audit view of neural decisions through explicit case-based evidence.

The account is exact for fixed-representation OLS readouts and audits the original network only to the extent of probe fidelity. The real-covariate experiments use synthetic or proxy action returns, and large training memories may require approximations such as Nyström. Extending the analysis to end-to-end nonlinear heads and estimated counterfactual returns remains future work.

References

[1] Alejandro Barredo Arrieta, Natalia Diaz-Rodriguez, Javier Del Ser, Adrien Bennetot, Siham Tabik, Alberto Barbado, Salvador Garcia, Sergio Gil-Lopez, Daniel Molina, Richard Benjamins, Raja Chatila, and Francisco Herrera. Explainable artificial intelligence (XAI): Concepts, taxonomies, opportunities and challenges toward responsible AI. *Information Fusion*, 58:82–115, 2020. doi: 10.1016/j.inffus.2019.12.012.

[2] Erico Tjoa and Cuntai Guan. A survey on explainable artificial intelligence (XAI): Toward medical XAI. *IEEE Transactions on Neural Networks and Learning Systems*, 32(11):4793–4813, 2021. doi: 10.1109/TNNLS.2020.3027314.

[3] Marco Tulio Ribeiro, Sameer Singh, and Carlos Guestrin. "why should i trust you?" explaining the predictions of any classifier. In *Proceedings of the 22nd ACM SIGKDD International Conference on Knowledge Discovery and Data Mining*, pages 1135–1144, 2016. doi: 10.1145/2939672.2939778.

[4] Scott M. Lundberg and Su-In Lee. A unified approach to interpreting model predictions. In *Advances in Neural Information Processing Systems*, volume 30, pages 4765–4774, 2017.

[5] Itzhak Gilboa and David Schmeidler. Case-based decision theory. *The Quarterly Journal of Economics*, 110 (3):605–639, 1995. doi: 10.2307/2946694.

[6] Itzhak Gilboa and David Schmeidler. *Case-Based Predictions: An Axiomatic Approach to Prediction, Classification and Statistical Learning*. World Scientific, 2012. doi: 10.1142/8243.

[7] Jared M. Hotaling, Chris Donkin, Andreas Jarvstad, and Ben R. Newell. MEM-EX: An exemplar memory model of decisions from experience. *Cognitive Psychology*, 138:101517, 2022. doi: 10.1016/j.cogpsych.2022.101517.

[8] Sebastian Olschewski, Aaron Luckman, Ashley Mason, Elliot A. Ludvig, and Emmanouil Konstantinidis. The future of decisions from experience: Connecting real-world decision problems to cognitive processes. *Perspectives on Psychological Science*, 19(1):82–102, 2024. doi: 10.1177/17456916231179138.

[9] Oriol Vinyals, Charles Blundell, Timothy Lillicrap, Koray Kavukcuoglu, and Daan Wierstra. Matching networks for one shot learning. In *Advances in Neural Information Processing Systems*, volume 29, pages 3630–3638, 2016.

[10] Chaofan Chen, Oscar Li, Chaofan Tao, Alina Barnett, Cynthia Rudin, and Jonathan K. Su. This looks like that: Deep learning for interpretable image recognition. In *Advances in Neural Information Processing Systems*, volume 32, 2019.

[11] Tom N. Wolf, Fabian Bongratz, Anne-Marie Rickmann, Sebastian Poelsterl, and Christian Wachinger. Keep the faith: Faithful explanations in convolutional neural networks for case-based reasoning. *Proceedings of the AAAI Conference on Artificial Intelligence*, 38(6):5921–5929, 2024. doi: 10.1609/aaai.v38i6.28406.

[12] Pavithra Pradeep, Monica Caro-Martinez, and Anjana Wijekoon. A practical exploration of the convergence of case-based reasoning and explainable artificial intelligence. *Expert Systems with Applications*, 255:124733, 2024. doi: 10.1016/j.eswa.2024.124733.

[13] Sascha Saralajew, Ashish Rana, Thomas Villmann, and Ammar Shaker. A robust prototype-based network with interpretable RBF classifier foundations. *Proceedings of the AAAI Conference on Artificial Intelligence*, 39(19): 20273–20282, 2025. doi: 10.1609/aaai.v39i19.34233.

[14] Guillaume Alain and Yoshua Bengio. Understanding intermediate layers using linear classifier probes, 2017.

[15] Kiho Park, Yo Joong Choe, and Victor Veitch. The linear representation hypothesis and the geometry of large language models. In *International Conference on Machine Learning*, 2024.

[16] Pang Wei Koh and Percy Liang. Understanding black-box predictions via influence functions. In *International Conference on Machine Learning*, pages 1885–1894, 2017.

[17] Chih-Kuan Yeh, Joon Kim, Ian En-Hsu Yen, and Pradeep Ravikumar. Representer point selection for explaining deep neural networks. In *Advances in Neural Information Processing Systems*, volume 31, 2018.

[18] Amirata Ghorbani and James Zou. Data shapley: Equitable valuation of data for machine learning. In *International Conference on Machine Learning*, volume 97 of *Proceedings of Machine Learning Research*, pages 2242–2251, 2019.

[19] Garima Pruthi, Frederick Liu, Mukund Sundararajan, and Satyen Kale. Estimating training data influence by tracing gradient descent. In *Advances in Neural Information Processing Systems*, volume 33, 2020.

[20] Andrea Schioppa, Polina Zablotskaia, David Vilar, and Artem Sokolov. Scaling up influence functions. *Proceedings of the AAAI Conference on Artificial Intelligence*, 36 (8):8179–8186, 2022. doi: 10.1609/aaai.v36i8.20791.

[21] Sung Min Park, Kristian Georgiev, Andrew Ilyas, Guillaume Leclerc, and Aleksander Madry. TRAK: Attributing model behavior at scale. In *International Conference on Machine Learning*, volume 202 of *Proceedings of Machine Learning Research*, pages 27074–27113, 2023.

[22] Juhan Bae, Wu Lin, Jonathan Lorraine, and Roger Grosse. Training data attribution via approximate unrolled differentiation, 2024.

[23] Zayd Hammoudeh and Daniel Lowd. Training data influence analysis and estimation: A survey. *Machine Learning*, 113(5):2351–2403, 2024. doi: 10.1007/s10994-023-06495-7.

[24] Xinyi Tian, Rachael Hwee Ling Sim, Jing Fan, and Bryan Kian Hsiang Low. DeRDaVa: Deletion-robust data valuation for machine learning. *Proceedings of the AAAI Conference on Artificial Intelligence*, 38(14): 15373–15381, 2024. doi: 10.1609/aaai.v38i14.29462.

[25] Han Zhang, Zhuo Zhang, Yi Zhang, Yuanzhao Zhai, Hanyang Peng, Yu Lei, Yue Yu, Hui Wang, Bin Liang, Lin Gui, and Ruifeng Xu. Correcting large language model behavior via influence function. *Proceedings of the AAAI Conference on Artificial Intelligence*, 39(13): 14477–14485, 2025. doi: 10.1609/aaai.v39i13.33586.

[26] Junwei Deng, Weijing Tang, and Jiaqi W. Ma. A versatile influence function for data attribution with non-decomposable loss. In *International Conference on Machine Learning*, volume 267 of *Proceedings of Machine Learning Research*, pages 13256–13276, 2025.

[27] Bruno Mlodozeniec, Runa Eschenhagen, Juhan Bae, Alexander Immer, David Krueger, and Richard E. Turner. Influence functions for scalable data attribution in diffusion models. In *International Conference on Learning Representations*, 2025.

[28] Cathy Jiao, Yijun Pan, Emily Xiao, Daisy Sheng, Niket Jain, Hanzhang Zhao, Ishita Dasgupta, Jiaqi W. Ma, and Chenyan Xiong. DATE-LM: Benchmarking data attribution evaluation for large language models. In *Advances in Neural Information Processing Systems*, volume 38, 2025.

[29] Jules Soria, Zakaria Chihani, Julien Girard-Satabin, Alban Grastien, Romain Xu-Darme, and Daniela Cancila. Formal abductive latent explanations for prototype-based networks. *Proceedings of the AAAI Conference on Artificial Intelligence*, 40(30):25590–25598, 2026. doi: 10.1609/aaai.v40i30.39755.

[30] Roger A. Horn and Charles R. Johnson. *Matrix Analysis*. Cambridge University Press, 2 edition, 2013.

[31] Stephen Boyd and Lieven Vandenberghe. *Convex Optimization*. Cambridge University Press, 2004. doi: 10.1017/CBO9780511804441.

[32] PJM Interconnection. Hourly metered load, data miner 2, 2024. URL https://dataminer2.pjm.com.

[33] I-Cheng Yeh and Che-hui Lien. The comparisons of data mining techniques for the predictive accuracy of probability of default of credit card clients. *Expert Systems with Applications*, 36(2):2473–2480, 2009. doi: 10.1016/j.eswa.2007.12.020.

[34] Dheeru Dua and Casey Graff. UCI machine learning repository, 2019. URL https://archive.ics.uci.edu/.

[35] Christopher K. I. Williams and Matthias Seeger. Using the Nyström method to speed up kernel machines. In *Advances in Neural Information Processing Systems*, volume 13, pages 682–688, 2001.

[36] Petros Drineas and Michael W. Mahoney. On the Nyström method for approximating a gram matrix for improved kernel-based learning. *Journal of Machine Learning Research*, 6:2153–2175, 2005.

Appendix A Notation

Appendix A collects the notation used across the theory, audit signals, and experiments. Table A1 lists the symbols needed to follow the decomposition, diagnostics, and supplementary analyses.

Symbol	Meaning	Symbol	Meaning
P, A, R	Problem, action, and return spaces.	$c = (p_c, a_c, r_c)$	A CBDT case.
M	A CBDT memory.	$U(a \mid M, p)$	CBDT support of action a in memory M.
$n(c, M)$	Frequency of case c in memory M.	$s(p, p_c)$	Problem-level similarity.
$u(r_c, a)$	Outcome support contributed by case c.	$\varphi(x) \in \mathbb{R}^H$	Fixed neural representation.
x_i or i	Training input or case index i.	n	Number of training cases.
H	Representation dimension or hidden width.	Φ	Training representation matrix.
$G = \Phi^\top \Phi$	Empirical uncentered Gram matrix.	I_H	H-dimensional identity matrix.
$Q(x, a)$	Network action score.	v_a	Linear readout weight for action a.
$\mathbf{r}_a$	Action-conditional return vector.	$r_i(a)$	Training-case return under action a.
$\alpha_i(x)$	OLS-induced case-influence coefficient.	$\alpha(x)$	Vector of case-influence coefficients.
$\alpha_\lambda(x)$	Regularized case-influence coefficient.	λ	Tikhonov regularization strength.
$\psi_i(a, x)$	Case audit contribution.	$I_k(x, a)$	Top-k case set for action-level influence.
$m_i(a, x)$	Absolute influence mass.	$\pi_k(b \mid x, a)$	Top-k absolute-mass action distribution.
a_i^*	Case-optimal action for case i.	$H_\alpha(x, a)$	Influence entropy for action coherence.
$q_x(a)$	Top-10 action distribution.	$D_{Gini}(x)$	Top-10 action-disagreement Gini.
$O_\alpha(x)$	Case-influence risk score.	γ	Weight on the Gini term in the risk score.
ε	Smoothing or numerical safeguard constant.	B	Invertible coordinate transform.
G_B	Gram matrix after coordinate reparameterization.	μ	Lagrange multiplier in the minimum-norm proof.
$T_{10}(x)$	Top-10 selected case set.	$L(v_a)$	Squared-loss or regularized objective.
ρ_{support}	CBDT-support alignment correlation.	ρ_{recon}	OLS–NN score-reconstruction correlation.
y	Observed binary label in UCI proxy audits.	a_0, a_1, a_2	Proxy action labels in tabular audits.
$PAY_0, \ldots, PAY_6$	Repayment-status feature in UCI Default Credit.	m	Nyström sampled-column count.

Appendix B Proofs and Derivations

Appendix B gives the algebraic details behind the theoretical claims in Sec. 3. It verifies the decomposition, coordinate invariance, and whitening sufficient regime.

B.1 Canonical OLS-Induced Decomposition (Proposition 1)

This proof derives the OLS case-influence decomposition and the minimum-norm characterization used in Proposition 1 and Sec. 3.1.

Step 1 — first-order condition

The squared-loss objective in Eq. (6) is $L(v) = \|\Phi v - r_a\|^2 = (\Phi v - r_a)^\top (\Phi v - r_a)$. Differentiating with respect to v gives $\nabla_v L = 2\Phi^\top \Phi v - 2\Phi^\top r_a$; setting this to zero yields the normal equation $\Phi^\top \Phi v = \Phi^\top r_a$, which is Eq. (7).

Step 2 — solving the linear system

Because Φ has full column rank, $G = \Phi^\top \Phi$ is invertible, so $v_a = G^{-1}\Phi^\top \mathbf{r}_a$ is the unique solution. Substituting into $Q(x, a) = v_a^\top \varphi(x)$ gives

$$Q(x, a) = \mathbf{r}_a^\top \Phi G^{-1} \varphi(x), \tag{21}$$

using the symmetry of G so that $G^{-\top} = G^{-1}$. Defining the coefficient vector $\alpha(x) = \Phi G^{-1}\varphi(x) \in \mathbb{R}^N$ yields the case-weighted form in Eqs. (9) and (10).

Step 3 — minimum-norm characterization

It remains to show that $\alpha(x)$ is the unique minimum-norm solution to $\Phi^\top \beta = \varphi(x)$. The Lagrangian is $L(\beta, \mu) = \| \beta \|_2^2 + \mu^\top (\Phi^\top \beta - \varphi(x))$. The KKT conditions [31] are $2\beta + \Phi\mu = 0$ and $\Phi^\top \beta = \varphi(x)$. From stationarity, $\beta = -\Phi\mu/2$; substituting into feasibility gives $-G\mu/2 = \varphi(x)$, so $\mu = -2G^{-1}\varphi(x)$. Therefore $\beta = \Phi G^{-1}\varphi(x) = \alpha(x)$. Strict convexity of $\| \beta \|_2^2$ and linearity of the constraint imply uniqueness.

Step 4 — Tikhonov-regularized case

Adding $\lambda \| v \|_2^2$ to the objective gives $L_\lambda(v) = (\Phi v - \mathbf{r}_a)^\top (\Phi v - \mathbf{r}_a) + \lambda v^\top v$. Setting the gradient to zero yields $(G + \lambda I_H) v_a = \Phi^\top \mathbf{r}_a$, and the analogous substitution produces Eq. (11). As $\lambda \to 0$, $(G + \lambda I_H)^{-1} \to G^{-1}$ whenever G is invertible, so the regularized coefficient converges to Eq. (10). ■

B.2 Coordinate Invariance (Section 3.2)

This derivation shows why the unregularized coefficient is invariant to invertible coordinate changes and why isotropic regularization breaks that property unless the metric is co-transformed.

Under the reparameterization $\varphi'(x) = B\varphi(x)$ with invertible $B \in \mathbb{R}^{H\times H}$, the new feature matrix is $\Phi' = \Phi B^\top$ and the new Gram matrix is $G' = \Phi'^\top\Phi' = B\Phi^\top\Phi B^\top = BGB^\top$. Hence $G'^{-1} = B^{-\top}G^{-1}B^{-1}$. Substituting into the OLS-induced coefficient,

$$\alpha_i'(x) = (B\varphi(x))^\top G'^{-1}B\varphi(x_i) = \alpha_i(x). \tag{22}$$

Since the transformed factors cancel algebraically, the equality in Eq. (22) follows. With Tikhonov regularization, the transformed original system expands to $B(G + \lambda I)B^\top$, whereas direct isotropic regularization in the new coordinates gives $BGB^\top + \lambda I$. These coincide only for orthogonal transforms. Otherwise, the coefficient remains invariant only when the regularization metric is co-transformed.

B.3 Whitening Sufficient Regime (Section 3.3)

This derivation locates a sufficient regime under which the OLS-induced coefficient reduces to scaled inner-product geometry and can match standard non-negative CBDT similarity semantics.

If $G = nI_H$, then $G^{-1} = (1/n)I_H$, and $\alpha_i(x) = (1/n)\varphi(x)^\top\varphi(x_i)$, the scaled inner-product. Non-negativity additionally imposes $\varphi(x)^\top\varphi(x_i) \geq 0$; a non-negative kernel (e.g. RBF, polynomial of even degree) supplies the standard CBDT non-negative similarity semantics.

Appendix C Additional Experiments

Appendix C provides auxiliary experiments and construction details for the empirical claims in Sec. 5. The subsections validate the similarity sufficient regime, explain signed coefficients, expand the single-decision audit, report the case-influence risk drift grid, define proxy returns, audit Default Credit, and test Nyström scaling. Appendix D separately reports the attribution timing and computational-cost details referenced in Sec. 5.3.

C.1 Post-Hoc Whitening Check for Coordinate Invariance

This check supports the coordinate-invariance analysis in Sec. 3.2 and the sufficient-regime discussion in Sec. 3.3. We apply post-hoc ZCA whitening before coefficient computation. Across five seeds, the negative-coefficient rate remains unchanged up to numerical precision, consistent with the claim that the unregularized coefficient is invariant under invertible reparameterization. The check does not use the whitening penalty as a training-time mitigation; it only verifies that coordinate whitening cannot by itself remove signed Gram coefficients.

C.2 Negative-Coefficient Geometry

This subsection supports the signed-coefficient analysis in Sec. 5.5 by aggregating the geometry of positive and negative coefficients over 50 PJM test inputs. The top-5 positive- and top-5 negative-coefficient training cases are extracted for each input. Mean φ-distance to the test input is 0.44 ± 0.04 for positive-coefficient cases and 3.30 ± 0.16 for negative-coefficient cases, a 7.5-fold distance ratio. The top-positive cases agree with the predicted action 64.1% of the time and have about 3.7 times larger absolute coefficient magnitude than the top-negative cases. Figure C1 visualizes the same coefficient-similarity relation: larger coefficient magnitudes concentrate at smaller representation-space distances, while distant cases mainly contribute weaker signed Gram corrections.

C.3 Case Audit Example: Single PJM Query

This subsection supports the single-decision audit in Sec. 5.5 by reporting the ranked cases behind the representative PJM test input shown in Figure 5. Network raw action scores are [-8.57, -6.20, -9.10], and the network selects action 1. Table C1 lists the strongest positive- and negative-coefficient cases. The top-5 positive-α training cases all lie within φ-distance 0.78 of the test input, whereas the top-5 negative-α cases all lie beyond φ-distance 3.73. The negative-coefficient cases are far-field references that the OLS normal equation subtracts through the inverse-Gram geometry.

The corresponding contribution values for the positive ranks are -0.0068 for all five cases, with match indicators yes, no, yes, yes, and yes. The negative ranks have contributions -0.0165, -0.0799, -0.0049, -0.0099, and 0.0024, with match indicators yes, no, no, no, and yes.

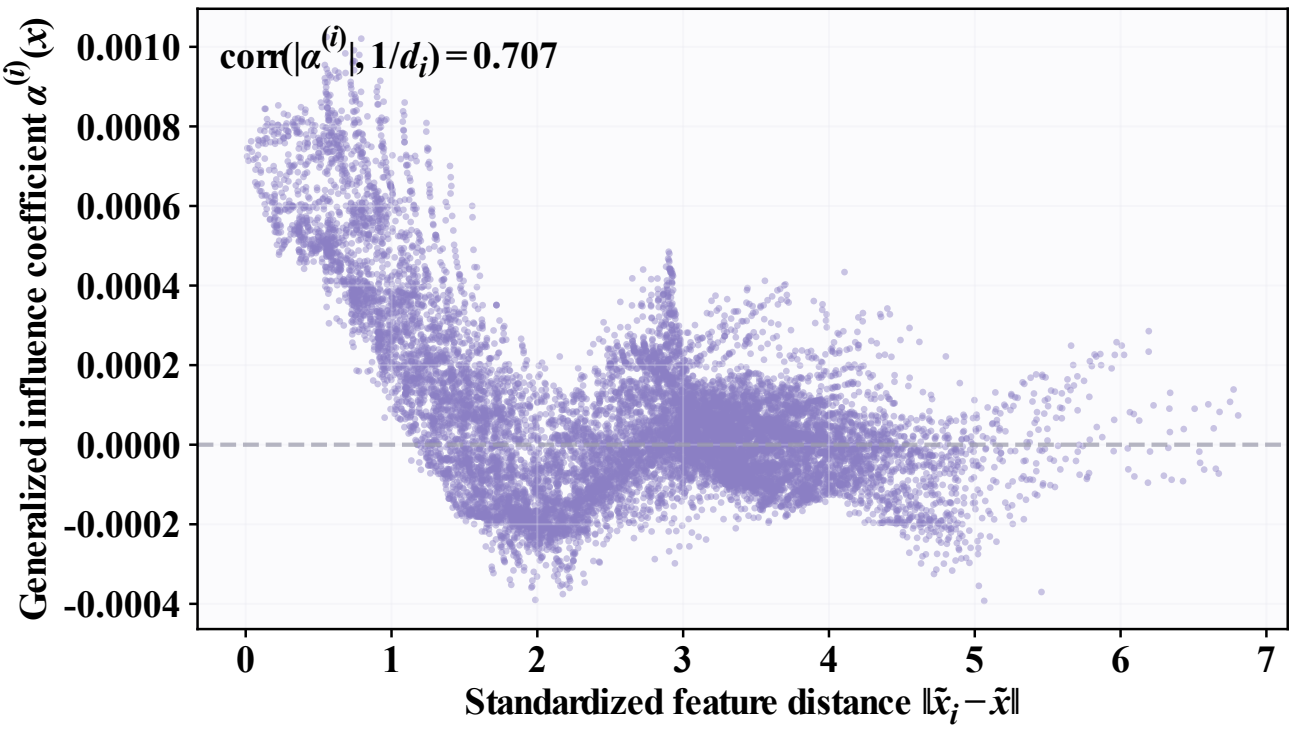

Figure C1: Alpha-distance relation. Large positive coefficients concentrate at small representation distances, while negative coefficients are farther away. This supports the audit view of nearby support cases and distant Gram corrections.

Grp.	Rank	Idx	α (unitless)	a^*	Ret. (proxy)	Dist. (repr.)
pos.	1	2860	**0.0011**	1	-6.000	**0.6531**
pos.	2	13072	**0.0011**	0	-6.000	**0.7589**
pos.	3	2262	**0.0011**	1	-6.000	**0.7672**
pos.	4	4102	**0.0011**	1	-6.000	**0.7319**
pos.	5	2814	**0.0011**	1	-6.000	**0.5428**
neg.	1	8338	-0.0004	1	39.243	**13.4546**
neg.	2	9304	-0.0004	2	193.323	**12.6168**
neg.	3	8292	-0.0004	0	11.944	**14.2427**
neg.	4	8246	-0.0004	0	24.474	**12.8511**
neg.	5	4280	-0.0004	1	-6.000	**4.8221**

Table C1: PJM case audit. Bold values mark the positive support coefficients and the near-versus-far distance pattern. The ranked list makes one neural decision inspectable through training cases.

C.4 Case-Influence Risk Diagnostic

This subsection supports the case-influence risk diagnostic in Sec. 5.5 by reporting the full drift grid behind the covariate-shift result. The diagnostic score defined in Eq. (20) is evaluated against the network-margin baseline on 27 drift configurations covering mean, variance, and covariate shifts over nine scale levels from 0 to 4.0, with five seeds for each configuration. Figure C2 reports the full grid.

The case-influence entropy and disagreement scores are most useful under covariate shift: from drift strength 2.0 onward, they consistently exceed the network-margin baseline in paired seed comparisons. Mean-shift differences are weaker, and variance shifts are better handled by the margin baseline. Figure C2 clarifies the operating regime: the score is most helpful when covariate shifts change local influential-case geometry and make case evidence more informative than a scalar margin.

Figure C3 reports the paired-seed significance test for the entropy score against the network-margin baseline. The strongest evidence appears under larger covariate shifts, supporting the main-text claim that the case-influence risk score captures changes in local influential-case geometry and action-evidence structure.

C.5 Proxy Return Construction

This subsection defines the proxy returns used by the UCI audits in Sec. 5.4. UCI Adult Income and UCI Default Credit provide labels only, so the experiments construct three-action proxy decision audits with controlled action-specific returns.

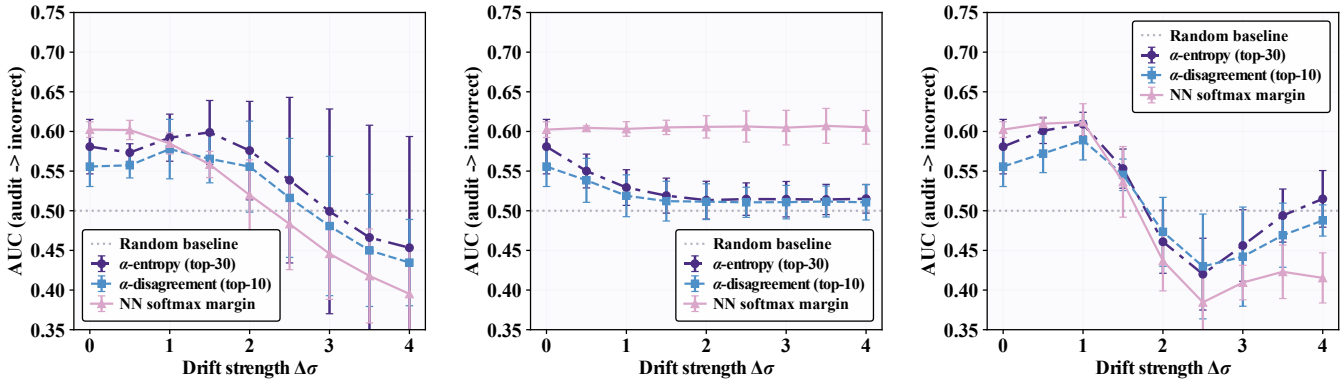

(a) Mean shift (b) Variance shift (c) Covariate shift

Figure C2: Case-influence risk drift grid. The case-influence diagnostic is strongest under covariate shifts, where influential neighborhoods change. This shows when case-level evidence adds value beyond margin confidence.

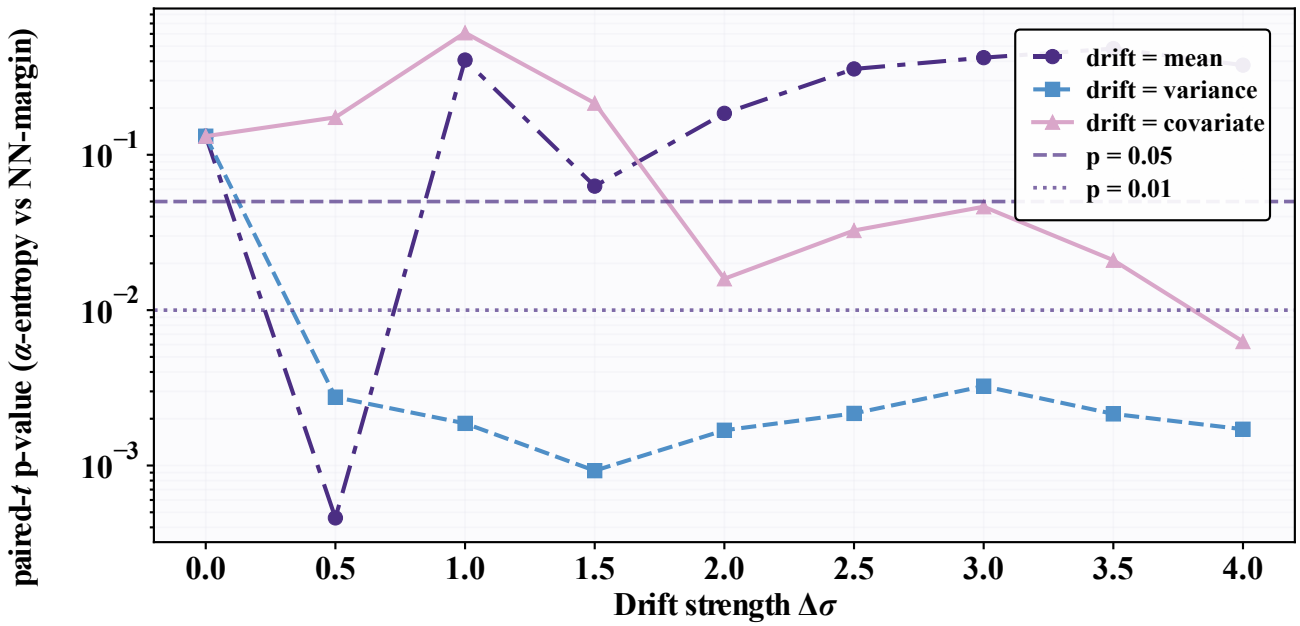

Figure C3: Paired risk comparison. Paired tests show the strongest gains under larger covariate shifts. The result supports using case-influence geometry as a complementary audit signal.

These returns evaluate the decomposition and audit signals under controlled specifications; deployment policy design would require independent return modeling.

UCI Adult Income

Three actions correspond to conservative reject (a_1), standard approval (a_2), and aggressive high-limit approval (a_3). Let y_i be the original (>50K) income label, $h_i = \mathbf{1}\{\text{education_num}_i \geq 13\}$, and $g_i = \mathbf{1}\{\text{capital_gain}_i > 0\}$. The return mapping is constructed so that the higher-risk action trades a larger upside for a larger downside:

$$
\begin{aligned}
r_i(a_1) &= 1 - 0.5y_i, \\
r_i(a_2) &= 0.5 + 0.4y_i, \\
r_i(a_3) &= -0.3 + 1.2y_i + 0.3h_i + 0.2g_i.
\end{aligned}
$$

A small Gaussian perturbation with standard deviation 0.05 is used only for tie breaking in the controlled audit. Return parameters were tested at 0.5-2 times the stated magnitudes, and the results are qualitatively unchanged.

UCI Default Credit

Three actions correspond to reject or decrease exposure (a_0), standard approval (a_1), and increase exposure (a_2). The default label "default payment next month" plays the role of y, where $y = 1$ denotes default. The proxy returns are

$$
\begin{aligned}
r_i(a_0) &= 0.5(1 - y_i), \\
r_i(a_1) &= 1 - 2y_i, \\
r_i(a_2) &= 2(1 - y_i) - 3y_i.
\end{aligned}
$$

This asymmetric mapping rewards greater exposure for non-default cases and penalizes it more heavily for default cases. Sub-memory splits are derived from AGE, SEX, EDUCATION, and recent-delinquency features; recent-delinquency is operationalized as $PAY_0 \geq 2$.

PJM bidding

PJM real half-hourly load observations define the state, and synthetic prices generate action-specific returns $r_i(a)$ for three bidding strategies (low, medium, and high). Because prices are synthetic, the per-action returns are directly observable for every training problem, satisfying the return-observation assumption of Sec. 2.2.

C.6 UCI Default Credit Decomposition Audit

This subsection supports the Default Credit component of Fig. 4 by providing the numeric decomposition audit behind the main-text summary. The audit uses 30,000 records with 23 features. Network-CBDT behavioral agreement is 0.8746±0.0047 over five seeds, and per-action OLS reconstruction correlations are 0.998±0.001, 0.956±0.032, and 0.998±0.001. The recent-delinquency split achieves the highest Gram mismatch in this dataset (approximately 0.91) while preserving A2 satisfaction near 1.0, making it a useful stress test for case-level evidence.

C.7 Nyström Scaling to Medium Hidden Width

This subsection examines computational scaling beyond exact inversion by replacing the exact regularized Gram inverse with a Nyström approximation that samples m columns of the feature matrix [35, 36] (rank fraction 0.50, with rank $H/2$). Five seeds are used, with hidden width $H \in \{32, 128, 512\}$. Table C2 reports timing and top-30 ranking overlap between exact and Nyström solutions. The overlap improves with representation dimension, and runtime gains appear from $H = 128$ onward in this implementation.

H	Rank	Exact (ms)	Nys. (ms)	Top-30 (prop.)	Pearson r
32	16	13.7±14.3	24.6±31.8	0.440±0.082	0.698±0.054
128	64	21.8±24.1	**11.1±0.7**	0.648±0.029	**0.731±0.021**
512	256	85.7±79.4	**68.3±0.9**	**0.793±0.024**	0.710±0.021

Table C2: Nyström approximation. Bold values mark the strongest approximation quality or the observed runtime gain at larger widths.

Appendix D Computational Cost

This appendix reports the computational cost of the attribution baselines used in the main comparison. The benchmark uses the same five seeds as the main attribution experiment and reports online per-query audit time after method-specific cached

quantities are available. Relative cost is normalized to the fastest method, Representer Point. Table C3 reports these values, and Figure C4 separates the two accuracy-side diagnostics used in the attribution comparison: Pearson support reconstruction and Top-30 action consistency.

Method	Time per query (ms)	Relative cost
Ours (α)	58.560±130.335	170.2×
Representer	0.344±0.110	1.0×
TracIn	0.494±0.088	1.4×
Influence Functions	0.503±0.073	1.5×

Table C3: Computational Cost of Attribution Baselines. Times are means with 95% confidence intervals over five seeds after method-specific cached quantities are available.

These measurements are implementation- and cache-dependent and should not be interpreted as optimized system-level benchmarks.

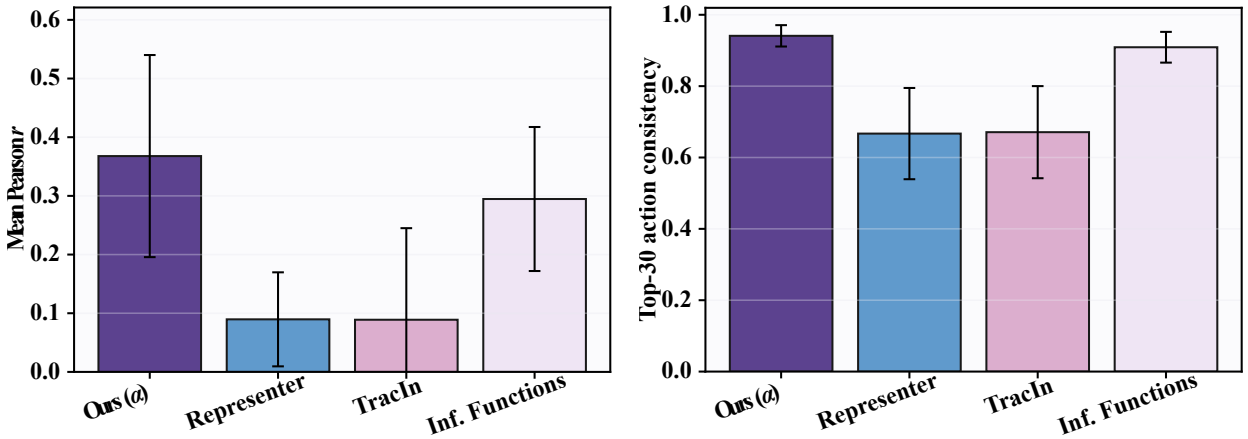

(a) Pearson reconstruction

(b) Top-30 consistency

Figure C4: Attribution diagnostic robustness. The panels summarize support reconstruction and Top-30 consistency. The proposed coefficient remains strongest on case ranking, reinforcing the main attribution result.